IOP Publishing Nuclear Fusion
Nuclear Fusion **XX** (XXXX) XXXXXX https://doi.org/XXXX/XXXX

An Overview of 3D Field Optimization for Control of Transport and Edge Instabilities on KSTAR

J. A. Snipes[1], J. Butt[2], C. S. Byun[2], T. Cote[3], K. Erickson[1], H. G. Frerichs[4], S. H. Hahn[5], Q. Hu[1], Y. M. Jeon[5], V. Khavin[6], M. Kim[2], S.K. Kim[1], M. W. Kim[5], W. H. Ko[5], E. Kolemen[2], N. Leuthold[7], Z. Lin[8], Y. Liu[6], N. C. Logan[7], P. Lunia[7], D. Orlov[6], G. Y. Park[5], J.K. Park[9], C. Paz-Soldan[7], A. Rothstein[2], G. W. Shin[5], R. Shousha[1], X. Sun[3], J. Van Blarcum[10], X. Wei[8], S.M. Yang[1], Y. Yu[8], C. Zhao[3], B. Zhu[11]

[1] Princeton Plasma Physics Laboratory, Princeton, NJ USA
[2] Princeton University, Princeton, NJ USA
[3] General Atomics, San Diego
[4] University of Wisconsin, Madison, WI USA
[5] Korea Institute of Fusion Energy, Daejeon, Republic of Korea
[6] University of California, San Diego, CA USA
[7] Columbia University, New York, NY USA
[8] University of California, Irvine, CA USA
[9] Seoul National University, Seoul, Republic of Korea
[10] ITER Organization, St. Paul-lez-Durance, France
[11] Lawrence Livermore National Laboratory, Livermore, CA USA

E-mail: jsnipes@pppl.gov

Abstract

An international team from several laboratories and universities has made key advances over the last few years in the control of plasma transport and edge instabilities with applied 3D fields in the KSTAR tokamak to optimize long pulse operation scenarios. This overview begins with the optimization of both core and edge resonant magnetic perturbations (RMP) to improve fast ion confinement to avoid excessive limiter heat loads due to fast ion losses and successful modeling of the experimental results. Integrated and advanced plasma control techniques with machine learning (ML) and adaptive control were then used to optimize the 3D field spectrum in real-time to control edge localized modes (ELMs) while avoiding core locked modes that could disrupt the plasma. Accelerating the offline model of 3D fields with a surrogate ML model can optimize ELM suppression in the edge while limiting the impact of the applied RMP fields deeper in the plasma core in real-time. In addition, the impact of the 3D fields on the divertor heat load has been modeled and compared with experimental measurements. An analysis of a multi-machine database including KSTAR has been performed to better understand the metrics for the observed RMP thresholds for ELM suppression and the resulting plasma performance. Predictive modeling of the operational space for ELM suppression and density pumpout due to RMP has shown the importance of magnetic islands in the plasma edge and their impact on plasma turbulence. This research has culminated in the development of successful long pulse operational scenarios on KSTAR while attempting to overcome challenges of the new tungsten divertor.

Keywords: KSTAR, plasma control, ELM suppression, 3D fields

1. Introduction

Achieving high plasma performance with sufficiently high particle and energy confinement while controlling the heat flux on plasma facing components is essential to achieve economic electricity production from fusion energy [1, 2]. In tokamaks, high confinement (H-mode) is robustly achieved in diverted magnetic configurations with sufficient input power and sufficiently low radiated power [3-7]. The most robust of these high performance regimes that ITER intends to use for its baseline Q=10 scenario is called the Type I ELMy H-mode regime [8, 9]. This regime is characterized by large instabilities known as Edge Localized Modes (ELMs) [10, 11] that eject particles and energy to the plasma facing components (PFCs) that can damage them due to excessive heat load at high performance. The scientific community has long sought ways to control, suppress, or mitigate ELMs to maintain high plasma performance and avoid excessive heat load to the PFCs [12-18]. One of the most successful control actuators has been the use of applied 3D magnetic fields to control edge stability and transport, which was pioneered on the DIII-D tokamak [13].

This paper is mainly an overview of the latest research advances over the past few years to model, control, suppress, and mitigate the impact of ELMs in the KSTAR tokamak by a large international team of researchers from several laboratories and universities. This overview begins with the optimization of both core and edge resonant magnetic perturbations (RMP) to improve fast ion confinement and avoid excessive limiter heat loads due to fast ion losses with successful modeling of the experimental results [19-25]. Some new results of fast ion loss modeling are also included in section 2. Such RMP optimization is then integrated into advanced plasma control techniques with machine learning (ML) and adaptive control to optimize the 3D field spectrum in real-time to control ELMs while avoiding core locked modes that could lead to disruptions [26-28]. Use of a surrogate Machine Learning (ML) model to accelerate the offline model of 3D fields optimizes ELM suppression in the edge while limiting the impact of the applied RMP deeper in the plasma core in real-time. The impact of the 3D fields on the divertor heat load has also been modeled and compared with experimental measurements [29, 30]. An analysis of a multi-machine database including KSTAR has been performed to better understand the metrics for the observed RMP thresholds for ELM suppression [31] and the resulting plasma performance [32]. Predictive modeling of the operational space for ELM suppression and density pumpout due to RMP fields has shown the importance of magnetic islands and neoclassical toroidal viscosity (NTV) [33-35] in the plasma edge and their impact on plasma turbulence [36]. Some new results of quasilinear MHD modeling of density pumpout are included in section 6. This work has culminated in the development of successful long pulse operational scenarios on KSTAR [37] while attempting to overcome challenges of the new tungsten divertor.

After summarizing these experimental and modeling results, ideas for future work to understand and mitigate the impact of tungsten on plasma performance in KSTAR are discussed.

2. Optimizing core and edge RMP fields for ELM control and fast ion confinement

The in-vessel correction coils on KSTAR [38] have a flexible configuration that is well suited to optimizing core and edge resonant magnetic perturbations. Figure1 shows the locations of the in-vessel correction coils on KSTAR, which include three rows of four coils each toroidally to provide up to n=2 perturbations, together with a simulation of an RMP normal field perturbation at the last closed flux surface that includes the ideal MHD plasma response.

Through sophisticated modeling of the plasma response of RMP fields and experimental validation, schemes for optimizing the 3D fields to maintain ELM suppression, avoid locked modes,

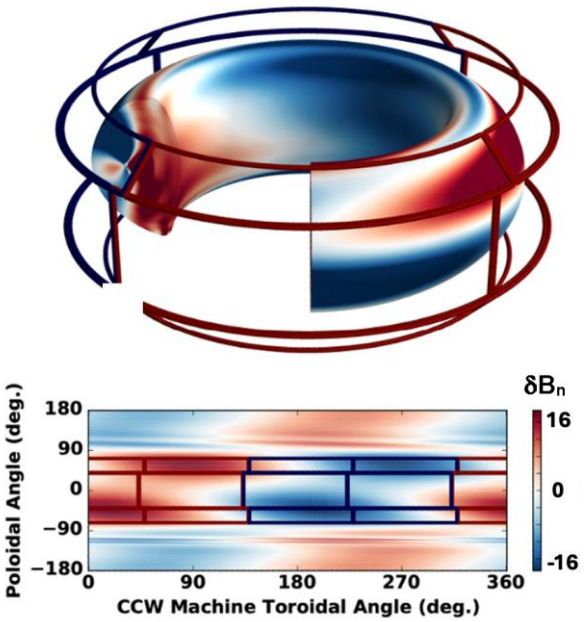

Figure 1. Location of the in-vessel correction coils on KSTAR in 3D and in 2D versus poloidal and toroidal angle together with a simulated normal field perturbation that includes the ideal MHD plasma response.

and improve the confinement of fast ions to avoid excessive heat loads to the KSTAR PFCs have been developed. The modeling has shown how to optimize the edge RMP (ERMP) perturbation to achieve and maintain ELM suppression while reducing the core RMP (CRMP) perturbation to improve fast ion confinement and avoid locked modes that can lead to disruptions [19-25].

Controlling fast ion losses can be as important as controlling ELMs to avoid excessive heating of the PFCs, particularly for long pulse high performance plasma operation. On KSTAR, fast ion losses are enhanced during RMP ELM suppression and can raise the limiter temperature to its limit of 600 °C, which then triggers an automatic shutdown of the plasma [21].

To understand the fast ion losses in the presence of RMP fields, the ideal plasma response to these fields is calculated with the Ideal Perturbed Equilibrium Code (IPEC) [39] and then used within the NuBDec code [40], which follows the guiding center orbits of the neutral beam injected (NBI) fast ions to calculate their deposition on the PFCs. Figure 2 compares two nearly identical KSTAR discharges with different poloidal phasing of the three rows of RMP coils. When comparing the vacuum resonant fields, both discharges had similar edge resonant fields, but shot 26026 had a much larger core resonant field than shot 26027. As can be seen in Figure 2, the different poloidal spectra of the two shots led to different plasma performance with a somewhat higher β_N in shot 26026. When including the plasma response with two different equilibria, which have different performance degradation by the different 3D field phasing, the resonant fields and normal fields are substantially larger in shot 26026 than in shot 26027. The resulting simulated fast ion losses for shot 26026 are much larger than for shot 26027. As can also be seen in Figure 2, the limiter temperature increases much more rapidly for shot 26026 than for 26027, indicating larger fast ion losses to the limiter for shot 26026. This is a result of the higher resonant

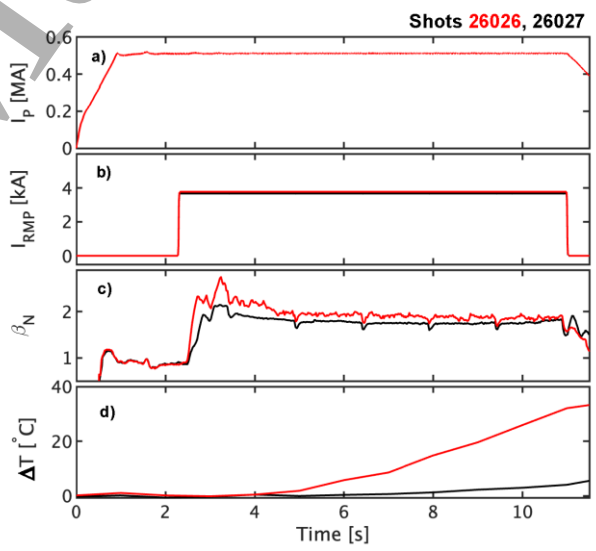

Figure 2. Comparison of two nearly identical KSTAR discharges with RMP ELM suppression except for the phasing of the RMP perturbation that provides nearly the same edge components, but much larger core component in shot 26026 showing a) plasma current, b) RMP current, c) β_N , d) change in limiter temperature vs time.

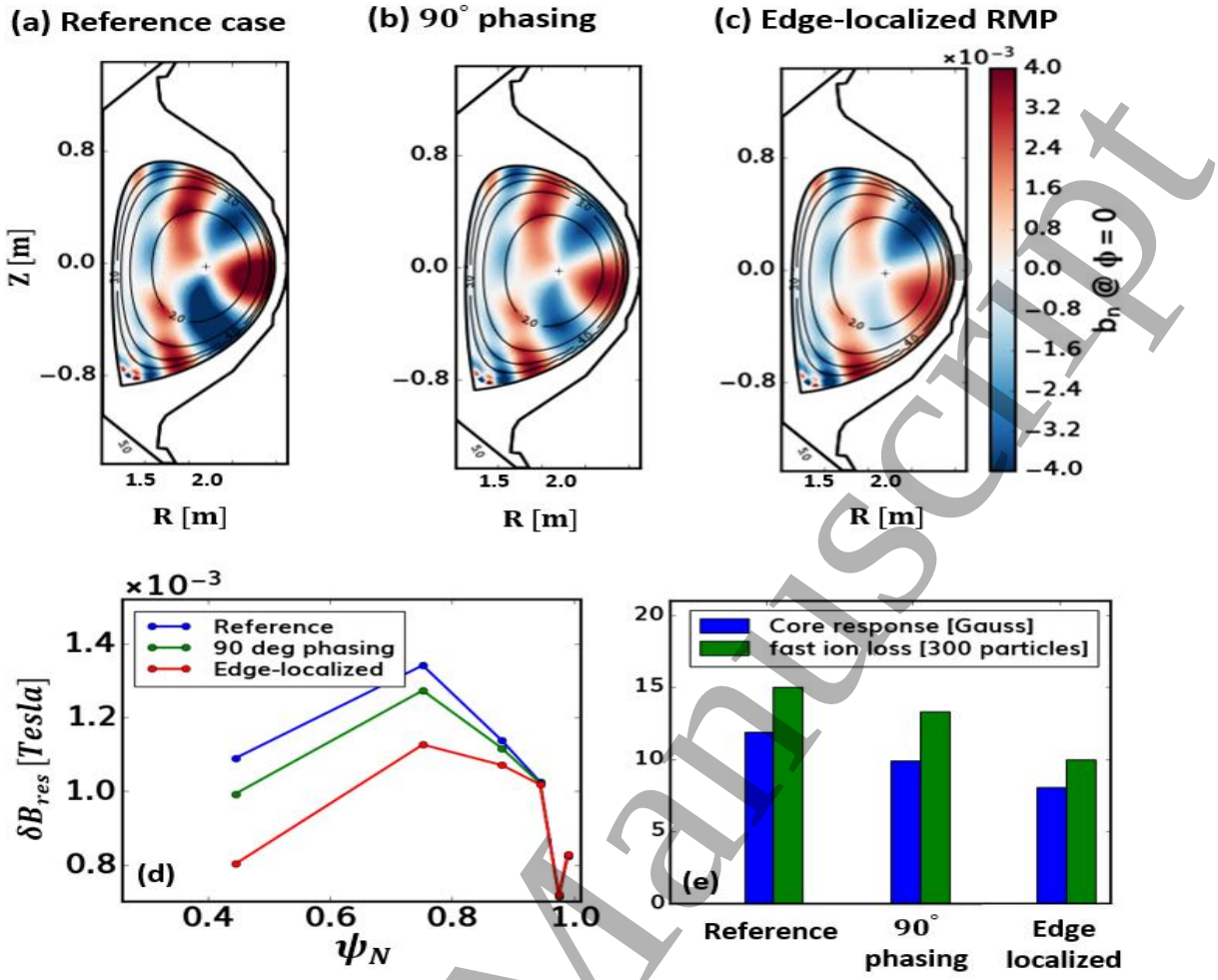

Figure 3. Comparison of the normal field perturbation in a) the reference case, b) the 90° phasing case, and c) the edge localized RMP case, and d) the resonant perturbed field radial profile vs normalized poloidal flux, and e) the ideal core resonant plasma response using GPEC and simulated fast ion loss for these three magnetic configurations. Fast-ion loss in (e) is computed using 200,000 Monte-Carlo particles for each case and is plotted in units of 300 particles (i.e., the plotted value ×300 gives the number of lost particles).

field amplification by plasma response from the different equilibria and slightly different β_N between the two discharges. This suggests a future experiment to determine how sensitive the plasma response is to slight changes in β_N and the resulting sensitivity to fast ion losses and resulting rate of rise of the limiter temperature.

Figure 3 compares the modeling of three different n=1 RMP phasing configurations for ELM suppression on KSTAR. In the reference configuration a), there is a sufficiently large edge resonant field in the pedestal region so that it is above the ELM suppression threshold using only currents in the top and midplane RMP coils. In the 90° phasing configuration b), there are equal currents in the top, middle, and bottom coils and the same toroidal phase difference $\phi_{TB} = \phi_{MB}$ for all three rows. This is the standard 3D field configuration for ELM suppression on KSTAR [19, 41, 42]. This configuration provides the same edge resonant field as in the reference case, but a significantly lower core resonant field. The third configuration c), provides an edge localized perturbation that optimizes the RMP fields for ELM suppression in the edge, but with a significantly

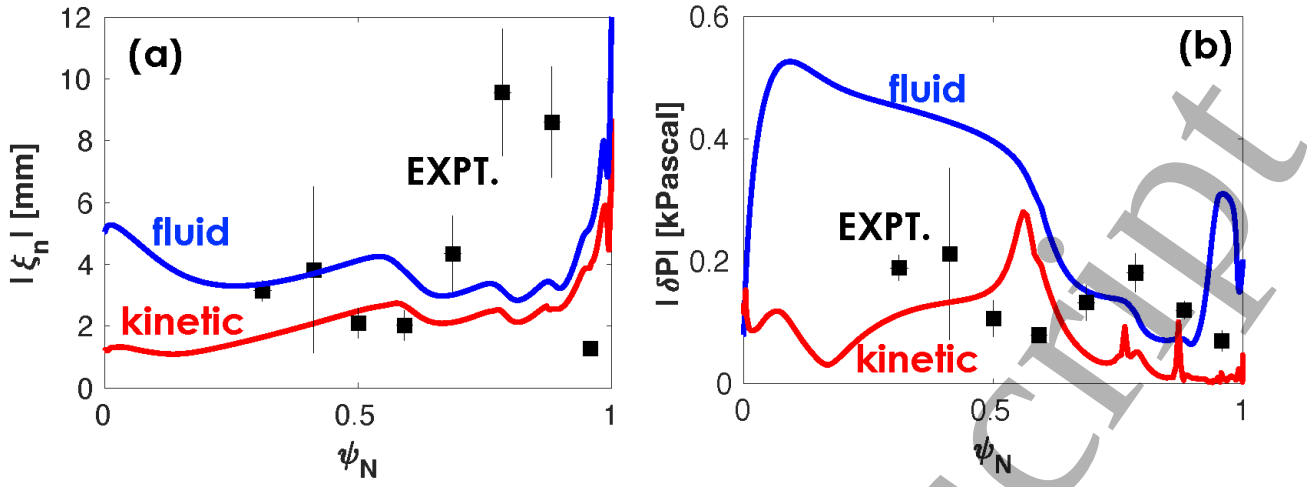

Figure 4. Comparison of MARS-F fluid modeling and MARS-K hybrid kinetic modeling with experimental measurements of a) the normal plasma displacement and b) the perturbed plasma pressure radial profiles vs normalized poloidal flux due to the RMP during ELM suppression on KSTAR.

smaller core perturbation. As can be seen in Figure 3d, all three configurations provide the same edge resonant field perturbation for ELM suppression, but a core resonant field perturbation reduced by 16% in the 90° phasing case and reduced by 32% in the edge-localized case. The associated toroidally averaged fast ion loss has also been calculated for all three configurations. The simulation results in Figure 3e show that a lower core resonant field leads to reduced fast ion loss. These results show that optimizing the edge resonant field for ELM suppression and reducing the core resonant field also leads to improved fast ion confinement.

The plasma response to the n=1 RMP fields used to suppress ELMs in KSTAR was also modeled with both the toroidal single fluid magnetohydrodynamic (MHD) code MARS-F [43] and the MHD-kinetic hybrid code MARS-K [44] to compute the RMP-induced fast ion losses [23]. Figure 4 shows the fluid and kinetic calculations of radial profiles of the perturbed normal plasma displacement due to the RMP $|\xi_n|$ and the perturbed plasma pressure $|\delta P|$ as a function of the normalized poloidal flux at the outboard midplane. In Figure 4, the MARS-F/K modeling is also compared with the measured plasma displacement in the perturbed electron temperature profile from electron cyclotron emission imaging (ECEI) [45] and the perturbed electron pressure calculated as $n_e\delta T_e$ from the interferometer line averaged density and ECEI measured electron temperature perturbation, assuming equal ion and electron temperature perturbations for the total pressure. As can be seen in Figure 4a, there is reasonable agreement in the core between the experimental measurements and the modeling of the plasma displacement, though both models underestimate the plasma displacement in the region near the top of the edge pedestal. The perturbed pressure in Figure 4b, shows reasonable agreement with the kinetic modeling, though a larger discrepancy with the fluid modeling.

New modeling results of fast ion losses in KSTAR due to RMP fields were modeled with the REORBIT code [46] for shot 30306 with n=1 RMP ELM suppression [23], assuming an initial 5D fast ion distribution (3D in real space and 2D velocity space). Figure 5 shows the REORBIT simulations comparing the final fast particle locations in the poloidal plane in (a) without RMP fields (labelled 2D) and (b) including RMP fields (labelled 3D). Figure 5(c) also shows the time traces of the fast

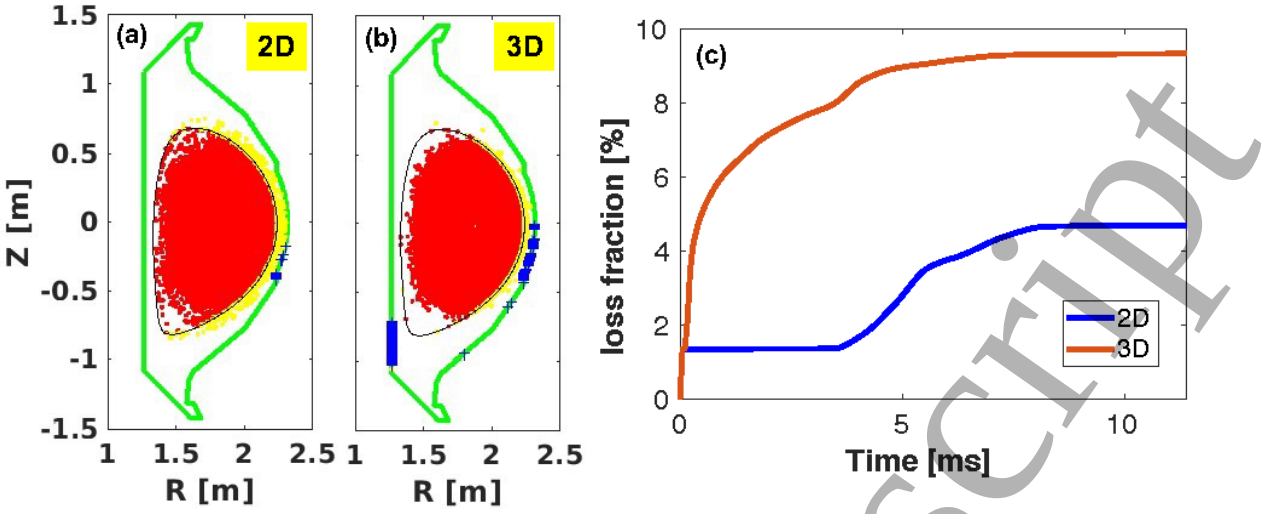

Figure 5. Fast ion losses modeled with REORBIT for KSTAR discharge 30306, assuming an initial 5D fast ion distribution. The final particle locations in the poloidal plane are compared (a) without, and (b) with, inclusion of the n=1 RMP 3D fields (red and yellow dots indicate confined particles while blue '+' indicate the strike locations of lost ions on the PFCs, and (c) compares time traces of the fast ion loss fraction without (blue 2D) and with RMP fields (red 3D).

particle loss fraction without (blue 2D) and with (red 3D) RMP fields. These simulations clearly show enhanced fast ion losses due to the applied n=1 RMP fields including the plasma response. The final loss fraction, defined with weights associated with the initial distribution function, is approximately doubled due to RMP (Figure 5(c)). More interestingly, lost fast ions due to RMP fields tend to strike a wider area of the PFCs including a region at the high-field side (Figure 5(b)). REORBIT also finds a non-uniform distribution of lost fast ions along the toroidal angle (not shown here).

This method of optimizing edge and core RMP perturbations can also reduce the risk of locked modes due to error fields and resulting disruptions by minimizing the core resonant perturbation [21]. Experiments were performed on KSTAR with currents programmed in the top row of error field correction coils to generate a known proxy n=1 error field and then vary currents in the middle and bottom rows of coils to correct the proxy error field. Figure 6 shows four different configurations of error field correction (EFC) in KSTAR. In the edge resonant EFC case shown in blue (26025), there remains a strong core error field that leads to a locked mode and disruption at about 3 s. In the

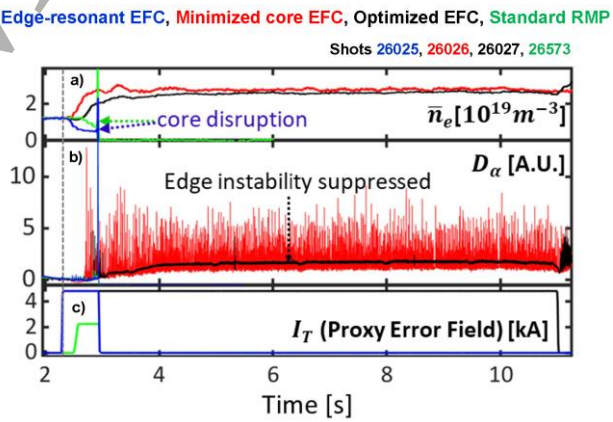

Figure 6. Comparison of four different error field corrections showing a) the line averaged density, b) the Da emission, and c) the top EFC coil current that generates the proxy error field. Edge-resonant EFC in blue (26025), minimized core EFC in red (26026), optimized EFC in black (26027), and standard RMP configuration in green (26573).

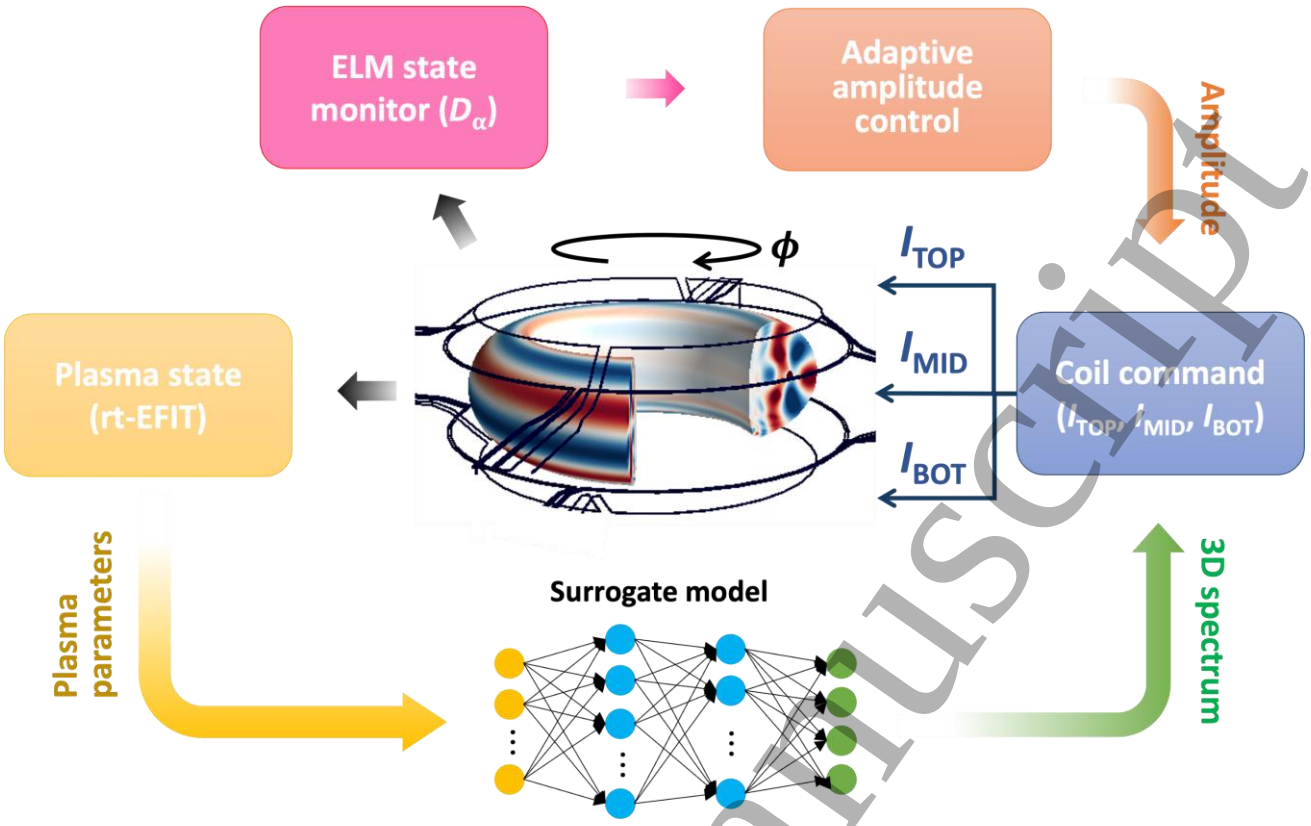

Figure 7. Schematic of the ML-3D adaptive model-based control algorithm that uses real-time equilibrium parameters in a fast surrogate machine learning based rt-IPEC model to set the RMP coil currents and phases adaptively depending on plasma conditions and the monitored ELM state.

minimized core EFC case shown in red (26026), the core error field is reduced, which avoids a locked mode, but the edge instability persists with large ELMs throughout the H-mode phase, as seen by the large spikes in D_α emission (Figure 6b). Then, in the optimized EFC case shown in black (26027), the core component is small enough to avoid a locked mode and the edge component is large enough to suppress ELMs throughout the H-mode. For comparison, a similar discharge with the standard RMP configuration for ELM suppression [19, 41, 42] is shown in green (26573), which has too large of a core error field, also leading to a locked mode and disruption. These examples clearly show the need to correctly tailor EFC to avoid disruptions, suppress ELMs, and maintain good thermal and fast ion confinement. In the subsequent sections of this paper, these core and edge RMP optimization techniques are applied in more sophisticated ways for real-time control to optimize plasma operation scenarios and extend high performance long pulse operation.

3. ELM control with 3D fields

A number of advanced control techniques have been employed to control the amplitude and phase of RMP fields to mitigate or suppress ELMs while reducing their impact on confinement in KSTAR. Real-time adaptive control of the RMP current amplitude and phase with a finite state machine design has been implemented to sustain ELM suppression while limiting the degradation in confinement that accompanies the application of RMP fields [28]. To avoid even a single ELM in a given discharge, a real-time ELM precursor detector based on an Interactive Multiple Model

Kalman filter approach [47, 48] enables the controller to act proactively before an imminent ELM. In addition, feedforward amplitude and phase control can allow the heat load to be spread across the PFCs by rotating the RMP fields with an adaptively reduced lower bound of RMP current to minimize the confinement degradation while maintaining ELM suppression despite changing plasma conditions. In addition, feedforward phase control to rotate the RMP fields effectively 'sweeps' the footprint of the heat flux across the divertor surface over time, which prevents localized overheating and mitigates damage to the PFCs (see section 4). The adaptive control balances the need to keep the RMP current above a minimum threshold to maintain ELM suppression while minimizing the RMP current, since too large an RMP current degrades confinement. In addition, a ML-based detector of the change from low to high confinement mode (L-H transition) was implemented [49] to rapidly increase the RMP current just after the L-H transition, since increasing the RMP current before the L-H transition can inhibit the transition to H-mode. This allows the controller to quickly suppress the first ELMs immediately after the L-H transition, which will be important in future high performance devices such as ITER [50].

Integrating these control improvements together has successfully improved plasma performance in KSTAR, as measured by the parameter $\beta_N = \beta_T a B_T / I_p$ where $\beta_T = \langle p \rangle / B_T^2 / 2\mu_0$ and $\langle p \rangle$ is the average plasma pressure. By maintaining the edge RMP (ERMP) field above the ELM suppresssion threshold while reducing the core RMP (CRMP) field to avoid locked modes from just after the L-H transition, improved confinement was achieved. The adaptive feedback controller optimizes the RMP current to maintain ELM suppression at the minimum current level to reduce confinement degradation, enhance β_N, and sustain the β_N-enhanced state. This integrated control succeeded in maintaining $\beta_N > 2.4$ for ~ 4 s

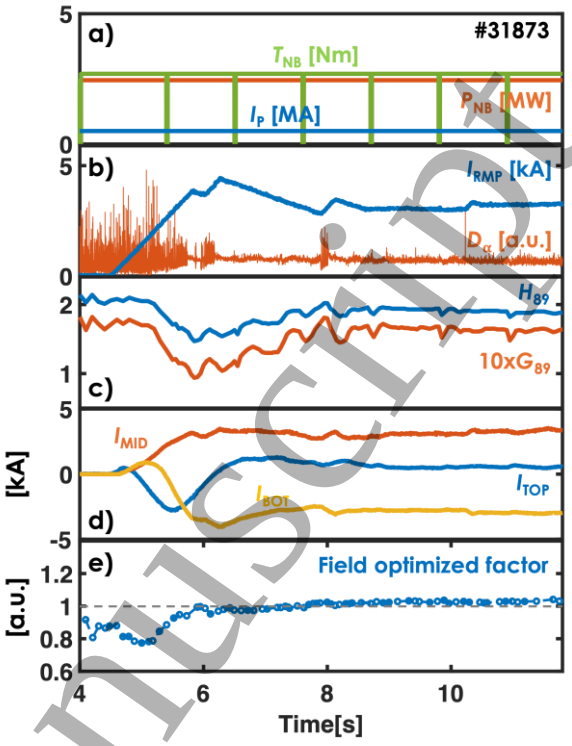

Figure 8. Data from KSTAR discharge #31873 where the ML-3D control algorithm demonstrates full feedback controlled optimized ELM suppression

(~60 τ_E) and achieved β_N transiently up to 2.65 during the ELM suppression phase [26].

To extend RMP control to future devices, a physics-based first principles approach has been used to determine the 3D waveform adaptively with changing plasma conditions for different devices. A ML technique was developed to automate 3D coil optimization based on the plasma equilibrium and ideal 3D response from IPEC simulations [20, 22, 39]. This approach has been validated across multiple machines [21, 22, 51] to predict the optimal 3D field configuration that minimizes the ratio B_{core}/B_{edge} of the core to edge perturbation to ensure ELM suppression while avoiding locked modes. These simulations, however, require tens of seconds of computational time, which prohibits real-time feedback control applications. To overcome these limitations, a surrogate machine learning-based model of IPEC was developed (ML-

3D) to speed up the calculations to ms timescales for real-time control [27]. The model was implemented into the KSTAR plasma control system (PCS) for real-time adaptive control. The model employs as inputs a number of parameters from real-time equilibrium calculations (the total plasma current (I_P), edge safety factor (q_{95}), global poloidal beta (β_P), global internal inductance (l_i), the coordinates of X-points on the R–Z plane (R_X, Z_X), and the plasma elongation (κ)). The outputs of the model are the RMP coil currents in the middle and bottom rows relative to the top row ($R_{M,B} = I_{M,B}/I_T$) and the top and bottom coil toroidal phases relative to the middle coil phase ($\phi_T = \phi_M - \phi_T$, $\phi_B = \phi_B - \phi_M$) (Figure 7). The model was trained on nearly 8500 existing KSTAR equilibria. The control algorithm adaptively changes the RMP current in real-time while monitoring the ELMs with a D_α signal. This maintains sufficient edge 3D field to access and maintain ELM suppression while simultaneously adjusting the current distribution among the RMP coils using the output of ML-3D to also guarantee a safe 3D field for disruption avoidance.

An example of the use of ML-3D is shown in Figure 8 for KSTAR discharge #31873 where the adaptive RMP coil control algorithm was triggered at 4.5 s. As can be seen in Figure 8a, the plasma current, neutral beam power and torque are held constant throughout this time period to ensure they do not change the confinement. Figure 8b shows, as the RMP current ramps up, the ELMs are stabilized in the D_α signal around 6.2 s. Initially, the confinement drops with increasing RMP current as seen in Figure 8c, where both the ITER 89P H factor above L-mode, H_{89} [52], is shown as well as the normalized fusion gain figure of merit $G_{89} = \beta_N H_{89}/q_{95}^2$ [53], where $\beta_N = \beta/(I/aB)$ and $\beta = p/(B^2/2\mu_0)$ is the ratio of kinetic to magnetic pressure in the plasma [2]. The feedback controlled top, middle, and bottom RMP coil currents are also shown in Figure 8d. The algorithm successfully suppresses ELMs automatically by 6.2 s with full feedback control and optimizes the three rows of RMP currents to reach and sustain a field optimized factor ~ 1 (Figure 8e) for safe ELM suppression for the rest of the discharge while avoiding disruptions. The field optimized factor is the ratio of the core to edge perturbed field produced by the ML-3D algorithm normalized to the core to edge field ratio obtained from an empirically established ELM suppression coil spectrum. By maintaining the field optimized factor ≤ 1, the algorithm ensures that the resulting perturbation spectrum corresponds to a relatively reduced core field compared to the edge field, as defined by the optimization metric. Furthermore, the initial drop in confinement due to high RMP current quickly recovers and maintains good confinement once the RMP current control is adaptively optimized. This feedback control scheme has the added benefit of optimizing 3D field control in real-time even for unexpected changes in conditions, which is essential for maintaining high performance long pulse discharges. Since ML-3D is a physics-based model, it can be easily extended to ITER and future fusion pilot plants.

4. Divertor performance with RMP ELM suppression

The impact of RMP fields on the heat load on the divertor is another critical issue for future magnetic confinement fusion devices since ELM suppression is intended to reduce the heat flux to PFCs to reduce erosion and extend their lifetime. Perturbations in the equilibrium magnetic field due to RMPs result in helical corrugations of the magnetic separatrix that appear as lobes in camera images of the X-point region [54], which lead to non-axisymmetric striations in the observed particle and heat flux measured on the divertor targets [55-57]. Controlling the broadening of these non-axisymmetric perturbations to the divertor heat flux while maintaining RMP ELM suppression is important to effectively mitigate the divertor heat flux. It was found experimentally that certain RMP spectra can broaden the divertor footprint while maintaining ELM suppression.

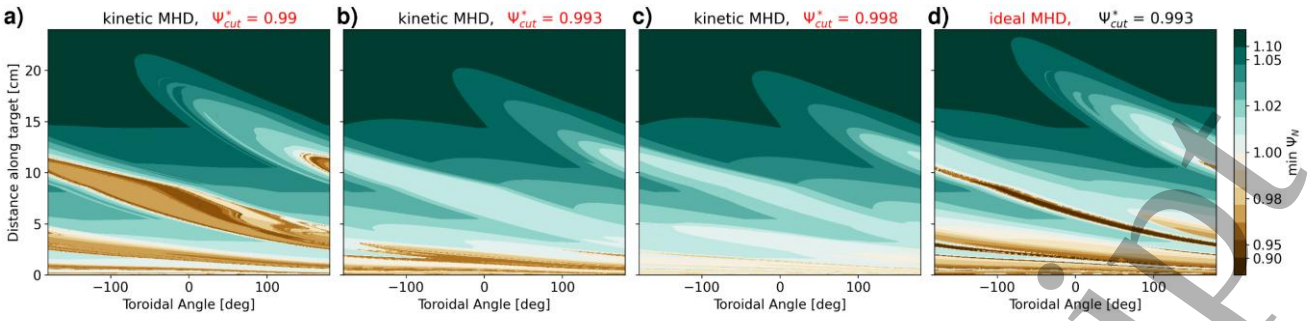

Figure 9. Magnetic footprint at the outer divertor target for three different values ψ_{cut}^* of the GPEC equilibrium truncation a) 0.99, b) 0.993, and c) 0.998 using with the kinetic MHD model and d) comparison with the ideal MHD model at ψ_{cut}^*=0.993.

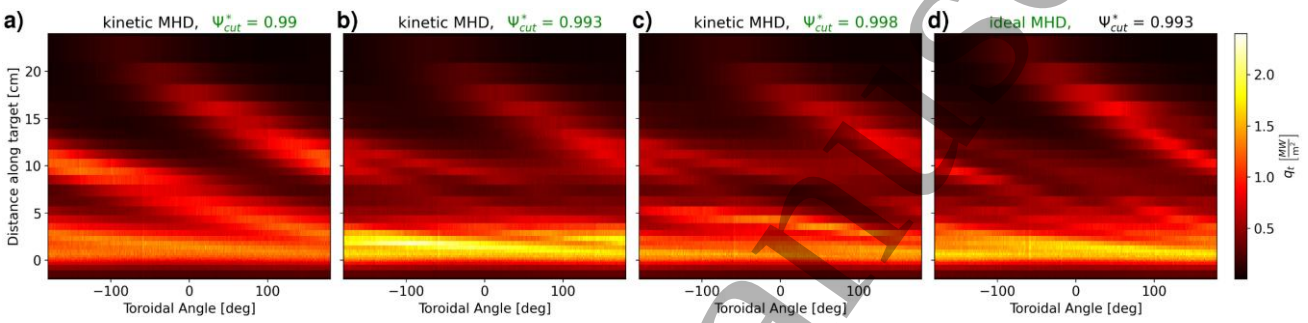

Figure 10. Calculated heat load on the outer divertor target for three different values ψ_{cut}^* of the GPEC equilibrium truncation a) 0.99, b) 0.993, and c) 0.998 using with the kinetic MHD model and d) comparison with the ideal MHD model at ψ_{cut}^*=0.993.

Modeling of the plasma response impact of RMP fields during ELM suppression on the divertor footprint for KSTAR has been performed [29] starting with stability analysis including the plasma response of an H-mode plasma that was previously carried out using the Generalized Perturbed Equilibrium Code (GPEC) [19]. The plasma boundary is modeled in steady-state, and the EMC3-EIRENE [59-61] code is applied to the perturbed magnetic field configuration. For an assumed fixed magnetic geometry, the field line tracing code FLARE [62] evaluates the radial connection of perturbed magnetic field lines from the divertor targets to the main plasma. The plasma response calculations from GPEC are plugged into the FLARE code and interpolated in the (R, Z) plane and extended toroidally with the toroidal mode number of the RMP perturbation for many RMP coil parameters. FLARE is then used to construct a mesh of finite flux tubes for each RMP configuration as input to the perturbed magnetic field for EMC3-EIRENE. The plasma density, temperature and parallel flow velocity are calculated by EMC3-EIRENE with recycling on the divertor targets and kinetic modeling of the neutral particles.

Since perturbed magnetic field lines can connect from the main plasma (normalized poloidal flux $\psi* < 1$) to the divertor targets, these perturbations to the field line affect the plasma and result in non-axisymmetric particle and heat loads on the divertor targets. Due to numerical issues at the separatrix, the GPEC calculations must be truncated at some value of $\psi* = \psi_{cut}^*$ just inside the separatrix. As seen in Figure 9, even small changes in this cut-off value (from 0.99, to 0.993, to 0.998) result in large

changes in the magnetic footprint on the outer divertor target. The figure compares the kinetic MHD model within GPEC at these three equilibrium truncation values with the results of the ideal MHD model at the intermediate value of 0.993. The colors in Figure 9 indicate the radial deviation in normalized poloidal flux of a field line from the corresponding equilibrium flux surface, where blue/green colors correspond to field lines that remain outside of the separatrix in the scrape-off layer while brown colors correspond to field lines that connect to the main plasma. To quantify the effect of the GPEC equilibrium truncation value on the magnetic footprint, we can define a footprint width s_{max} as the maximum distance along the divertor target from the equilibrium strike point to where field lines connect to the main plasma. Increasing ψ_{cut}^* from 0.99 to 0.993, decreases s_{max} from 12.0 cm to 3.2 cm and a further increase to 0.998 decreases s_{max} to 2.6 cm using the kinetic MHD model. If the ideal MHD model [39] is used (Figure 9d), a quite different striation pattern is found with s_{max} = 11.3 cm.

Simulations of the resulting divertor heat flux were performed with the EMC3-EIRENE code for the perturbed equilibria from Figure 9. As can be seen in Figure 10, quite different heat flux patterns result from the different equilibrium truncation values. Since truncation nearer to the separatrix includes more resonant flux surfaces, it is expected that the larger ψ_{cut}^* closer to 1 should provide a more realistic simulation and since the kinetic model includes more physics than the ideal model, the kinetic simulations are expected to be closer to the experiment.

These simulations have shown that small changes in the equilibrium truncation value within the last 1% of the normalized poloidal flux result in substantial differences in the striation patterns from field lines that connect from the main plasma to the divertor targets. The non-axisymmetric striation pattern tends to shrink with an increasing number of resonances in GPEC (i.e. truncation closer to the separatrix), but an extended analysis with higher resolution in both the equilibrium and plasma response is required to determine if this converges. Furthermore, significant differences are found between the calculated divertor footprints using ideal and kinetic MHD models in GPEC.

Erosion and redeposition of the divertor PFCs has also been calculated with the ERO2.0 code [63] for this magnetic configuration in KSTAR utilizing GPEC to calculate the perturbed equilibrium in the SOL ($0.9 < \psi^* < 1$) and EMC3-EIRENE to provide the input plasma background [30]. ERO2.0 takes into account physical sputtering, chemical erosion, material mixing, ionization, recombination, and deposition along the targets. These calculations were performed in the full carbon wall and divertor configuration. These results show that the largest net erosion occurs in the no-RMP reference case and the erosion and impurities in the plasma decrease with increasing RMP current. The magnetic footprint has a large effect on the resulting erosion of the divertor targets. The zones of net erosion are from the lower outer divertor target with redeposition on the remaining divertor targets in both the no-RMP and RMP cases. Since anomalous diffusion is the main transport mechanism for particles leaving the core plasma, improved core-edge integration is essential to properly model impurity transport.

5. RMP Thresholds for ELM suppression and operational space and performance

The RMP thresholds [31], operational space and plasma performance [32] of RMP ELM-suppressed plasmas were studied using a database of discharges from AUG, DIII-D, EAST, and KSTAR. The experimental threshold for achieving ELM suppression was compared for five metrics: (1) the island overlap width, (2) pedestal top Chirikov overlap, (3) peeling edge displacement, (4) pedestal top resonant drive, and (5) edge dominant mode overlap. In addition, two new first-principles

models of the threshold were compared with the database. The upper limit of the pedestal-top density for RMP ELM suppression in all of these devices is $\leq 3.5 \times 10^{19}$ m^{-3} [32]. The normalized plasma performance of these plasmas is found to be in an intermediate range of β_N and H_{89} within ITER expectations.

The threshold metric that appears to be the most robust in the database analysis [31] for projecting to new plasma scenarios is the dominant edge mode overlap (δ_e) normalized to the on-axis toroidal field, which is also a good metric for error field correction [64]. Another advantage of this metric is that it is not very sensitive to details of the equilibrium profiles. A critical vacuum island width metric at the pedestal top due to the RMP field including the plasma response was also found to have a similar distribution using the database as the edge overlap metric [31]. This metric should provide improved extrapolation outside the existing database for predictions to future fusion pilot plants.

The operating space across these four tokamaks for RMP ELM suppression covers a broad range of plasma parameters such as I_p, B_T, q_{95}, and plasma shape, even though, within a given device, the operating parameter ranges are restricted. All four of these machines, however, are mid-sized conventional aspect ratio tokamaks, so more data are needed from larger machines with RMP coils like ITER [65] and JT60-SA [66] to extend the range in data to larger size. Despite the broad range of some plasma parameters across these machines, the pedestal-top density has a seemingly fixed upper limit $\leq 3.5 \times 10^{19}$ m^{-3} [32].

In terms of plasma performance, the RMP ELM suppressed plasmas in the database [32] fall over a broad range of β_N up to 2.65 in KSTAR [26] and a broad range of energy confinement up to $H_{89} \sim 2$ relative to the L-mode scaling. Similarly, the database values relative to the ITER98,y2 H-mode confinement scaling [67] cover a broad range up to $H_{98,y2} > 1.3$. These values well exceed ITER

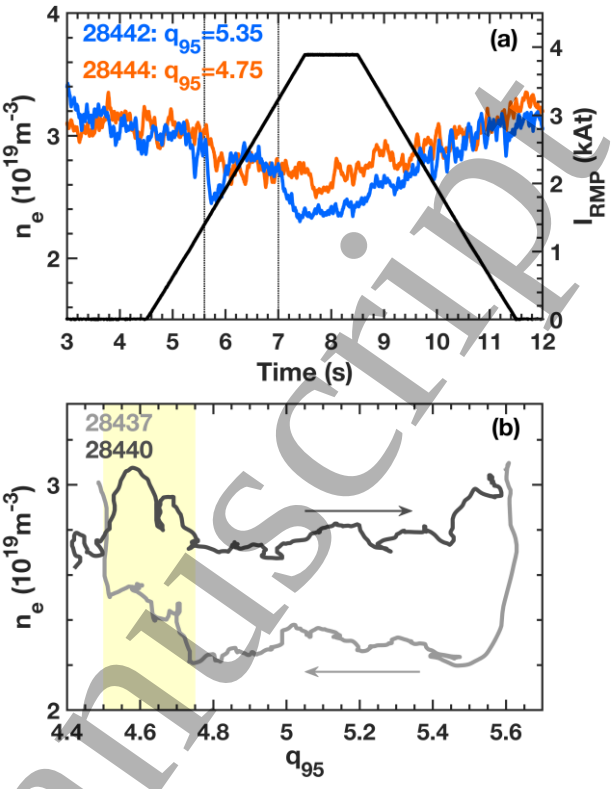

Figure 11. (a) Time trace of KSTAR discharges #28442 in blue and #28444 in red with n = 1 RMP, in terms of edge electron density and RMP coil current. The dashed lines show the time of bifurcation in density pump-out for #28442. (b) Edge density versus q_{95} for #28437 in grey and #28440 in black, and the yellow shaded region indicates the phase of partial recovery in density pumpout.

requirements for achieving Q=10, indicating that RMP ELM suppression scenarios should extrapolate well to high performance ITER operation.

6. RMP ELM suppression operational window prediction and density pumpout

There have been a number of attempts to predict the ELM suppression operational window and resulting reduction in the pedestal density ('density pumpout') due to RMP fields [68-72] assuming collisional or turbulent transport. RMP–driven magnetic islands in the pedestal region are also

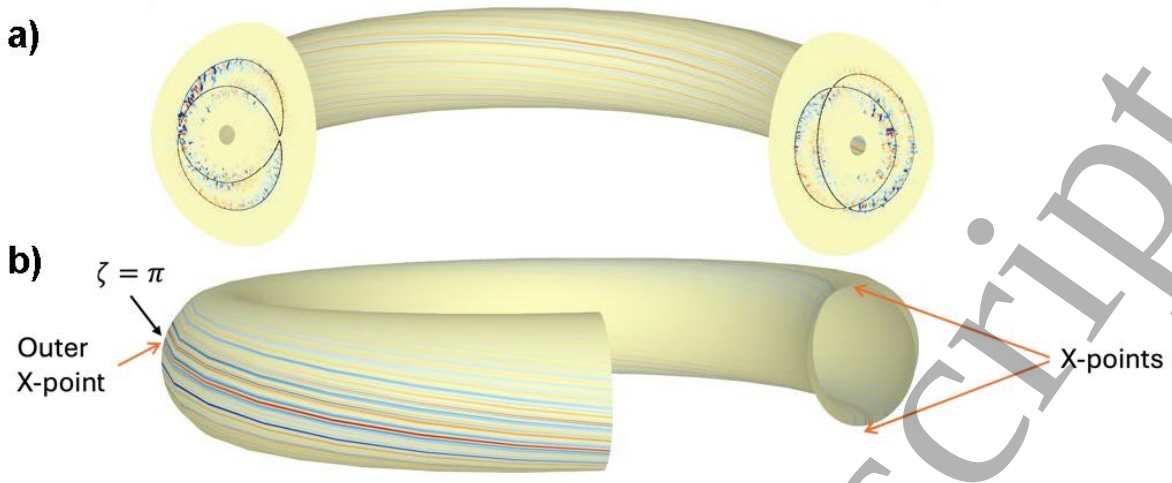

Figure 12. Normalized ion heat flux (Q_i) on different flux surfaces in the nonlinear steady state a) near the inner magnetic island separatrix (indicated by black lines) and b) at the q=2 surface. The poloidal planes at $\zeta=0$ and $\zeta=\pi$ are shown in panel a).

believed to play a central role in both ELM suppression and density pump-out. This motivated the design of dedicated experiments on KSTAR, complemented by nonlinear two-fluid simulations using the TM1 code [73, 74]. The TM1 simulations reveal key features of RMP-induced density pump-out via pedestal-foot island formation, including a bifurcation in pump-out with a low RMP coil current threshold and a strong sensitivity of the pump-out magnitude to q_{95} [34]. Gyrokinetic turbulence simulations of magnetic islands in KSTAR have also been performed and found quantitative agreement with experiment for time, frequency, and the perpendicular wavevector spectrum [36]. The quasi-linear initial value code MARS-Q [75] was also used to model density pumpout in KSTAR. In addition, nonlinear hybrid kinetic-MHD simulations with the JOREK code [76, 77] were carried out to model two-stage density pumpout [33].

To investigate these predictions, experiments were conducted on KSTAR using a controlled ramp-up and ramp-down of the middle row of RMP coil current while maintaining constant D_2 gas puffing. The coils were configured to produce n = 1 RMP fields, with only the middle row activated to trigger bifurcated density pump-out at higher current thresholds compared to the three-row configuration. An example of bifurcated density pump-out during the ramp-up of n = 1 RMP current is shown in Figure 11(a) for shot 28442 with constant q_{95} = 5.35. The coil current was increased gradually from 0 to 4 kAt over 3 s. Two distinct step-like bifurcations in edge line-averaged density were observed at 5.6 s and 7.0 s, corresponding to threshold currents of 1.45 kAt and 3.3 kAt, respectively. These observations are qualitatively consistent with TM1 predictions of bifurcated island formation. Notably, after the first bifurcation, the density partially recovered, correlated with a rapid change in toroidal rotation and ion temperature. During the subsequent coil ramp-down (8.5–11.5 s), the edge density gradually recovered. For comparison, discharge 28444 at q_{95} = 4.75 exhibited only a single bifurcation at 5.7 s, with smaller pump-out magnitude during the flattop compared to shot 28442. Another discharge at q_{95} = 5.05 (not shown) displayed one bifurcation with pump-out magnitude larger than that at q_{95} = 4.75

but smaller than at q_{95} = 5.35, again consistent with strong pump-out. Specifically, stronger pump-out

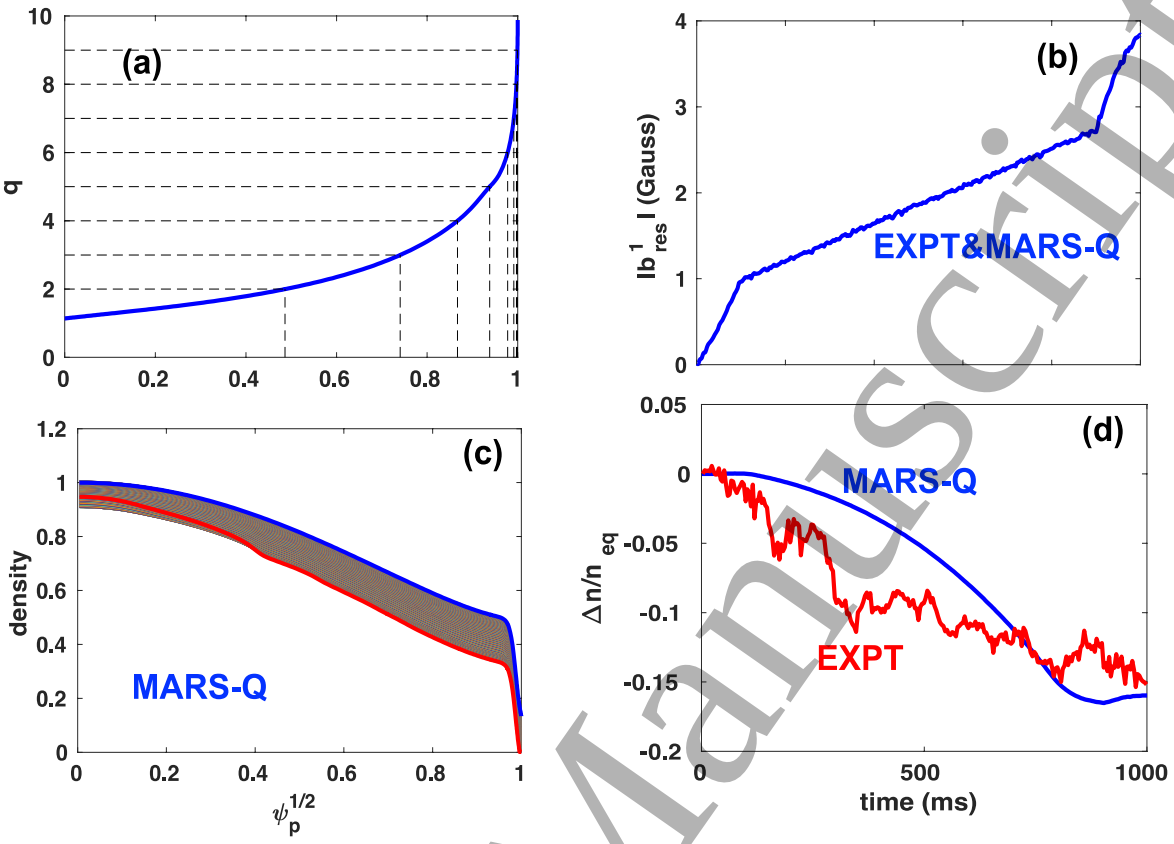

Figure 13. MARS-Q simulated density pumpout during the ELM suppression experiment in KSTAR discharge 30306, showing (a) the equilibrium safety factor, (b) the edge resonant field responding to the experimental RMP coil current ramp-up, (c) the modeled density profile evolution (thick blue: initial profile, thick red: final profile), and (d) the MARS-Q net density pumpout fraction compared to experiment.

TM1 predictions [34].

Further experiments with a continuous q_{95} scan were performed to document the specific q_{95} window for strong density pump-out at a constant RMP current of 4 kAt. Figure 11(b) shows the edge density dependence on q_{95} for shots 28437 and 28440. For shot 28437, an initial 30% density pump-out remained nearly constant as q_{95} decreased, then recovered to 20% as q_{95} was lowered into the window of 4.5–4.75 (shaded region). This weaker pump-out persisted until the end of the scan at q_{95} = 4.5. Shot 28440, with an upward q95 ramp, showed a similar window for occurred for q_{95} < 4.5 or q_{95} > 4.75, with partial density recovery within the 4.5–4.75 window. These results are qualitatively consistent with TM1 predictions [34], though baseline density levels differed between the two discharges.

Gyrokinetic simulations were used to examine how magnetic islands influence ion-temperature-gradient (ITG) turbulence in the KSTAR tokamak under resonant magnetic perturbations (RMP) [36]. The simulations indicate that turbulent transport is regulated by nonlinear coupling among ITG fluctuations, self-generated vortex flows, and zonal flows, producing anisotropic fluctuation and

transport patterns both in the poloidal plane and toroidally. The GTC code [75] was employed with realistic geometry and profiles from KSTAR long-pulse discharge #19118, which contains a large m/n = 2/1 magnetic island of about 4 cm width [76, 77] at the q = 2 surface produced by an n=1 RMP that suppresses ELMs. The island induces a significant enhancement in both ion and electron heat conductivities, consistent with a reduced steady-state zonal-flow level. Turbulence drives vortex flows along the island separatrix, which leads to temporal oscillations in the transport level and a redistribution of turbulence and transport in real space. Transport is strongest along the separatrix and is suppressed inside the island region. A toroidal variation in transport is also found. Because ITG turbulence has a strong ballooning structure, enhanced transport appears only when the magnetic island X-point aligns with the outer mid-plane, as shown in Figure 12.

New modeling of density pumpout in KSTAR (shot 30306) with the quasi-linear initial value code MARS-Q [78] has been performed for benchmarking validation. The RMP currents were applied with toroidal mode number n=1 to suppress Type-I ELMs, which resulted in density pumpout (red curve in Figure 13(d)) during the RMP coil current ramp-up phase (Figure 13(b)). The modeling results reported here assume plasma and RMP coil configurations as close as possible to the experimental conditions. The net density pumpout fraction is quantitatively recovered by the MARS-Q simulation (blue curve in Figure 13(d)), where various particle fluxes (including that associated with NTV [35]) due to 3D perturbations were considered. These results further validate the MARS-Q particle transport model in the presence of 3D fields.

Figure 14 shows another example of density pumpout in KSTAR during a ramp in n=1 RMP current for ELM suppression. One pumpout occurs at about 6.5 s, as seen by the drop in the electron density at the top of the pedestal in Figure 14b, and

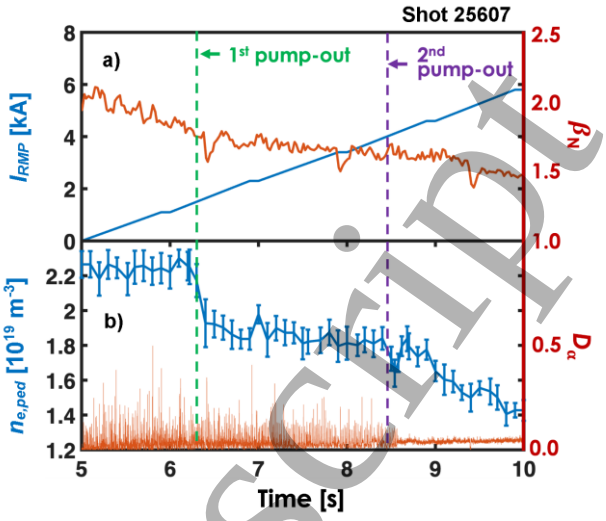

Figure 14. Time traces of KSTAR discharge #25607 showing a) the ramping n=1 RMP current and β_n and b) the D_α emission and the pedestal top electron density with two density pumpouts at just before 6.5 s and 8.5 s.

a second pumpout occurs at about 8.5 s, just as the ELMs are suppressed, as seen in the D_α emission near the outer strike point in Figure 14a. The pedestal top density quickly recovers after the second pumpout in ~100 ms. This is likely due to ELM suppression, which reduces the particle exhaust due to ELMs. Suppressing ELM crashes quickly restores the pedestal density. Changes in edge turbulence during ELM suppression could also be responsible for changes in particle transport that restored the pedestal density [81].

Nonlinear JOREK simulations with and without neoclassical toroidal viscosity [33] of the discharge in Figure 14 are able to simulate both density pumpouts with increasing RMP field, as found in experiment, at I_{RMP} = 1.5 kA and 4.0 kA. Each pumpout is triggered by the rapid growth of magnetic islands first at poloidal and toroidal mode numbers $m/n = 6/1$ and later at $m/n = 5/1$ as the RMP current increases. The simulations also predict the measured change in dn_e/dI_{RMP} at 1.5 kA and 4.0 kA with increasing magnetic island sizes. Including NTV in the simulation yields a density pumpout

that is quantitatively closer to the experimental values. The sudden increase in magnetic island sizes above a certain threshold in RMP current is well understood as field penetration [82], which happens multiple times as there are multiple rational surfaces, as indicated by the previous TM1 simulations. These nonlinear JOREK simulations provide additional particle transport dynamics due to island evolution in full geometry and access to ELM suppression.

7. Scenario development for long pulse steady-state operation

The integration of the work presented here into KSTAR plasma operation scenario development and real-time control algorithm development has led to record long RMP ELM suppressed high performance discharges up to 45 s duration [37]. The first essential ingredient was the optimization of the core and edge RMP spectrum with three rows of coils to maintain ELM suppression while avoiding both thermal and fast ion confinement degradation and locked modes in the core (as summarized in section 2). The next ingredients were the preemptive initiation of RMP using machine-learning detection of the L-H transition and adaptive ELM control with real-time D_α measurements (as summarized in section 3). Then, optimization of long pulse operation was essential to maintain ELM suppression. The RMP optimization with adaptive control was also important to avoid excessive heat loads on the PFCs by optimizing fast ion confinement during long pulse operation. The final limiting factor for long pulse operation was inductive flux consumption so that further optimization will require integrating non-inductive current drive scenarios. In addition, long pulse density control is essential to maintain ELM suppression and confinement at high plasma performance.

Figure 15 shows an example of long pulse RMP ELM suppression in KSTAR. Some issues that arise with long pulse ELM suppression include a

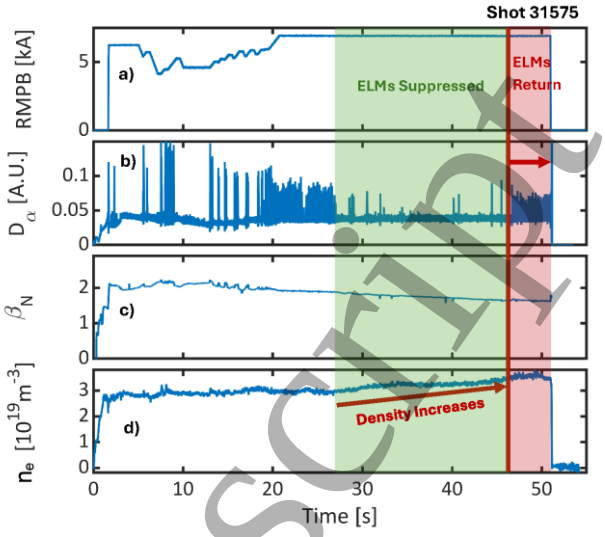

Figure 15. Time traces of KSTAR discharge #31575 showing a) the controlled bottom RMP coil current, b) with periods of ELM suppression and return to ELMs visible in the D_α emission and c) decreasing β_N and d) increasing electron density.

gradual increase in density (Figure 15d) and an accompanying degradation in confinement (Figure 15 c). In this case, the RMP current in the bottom row of coils saturates at the 5 kA limit of the power supplies and the increasing density cannot maintain ELM suppression with the RMP current available. The loss of density control may be due to saturation of the carbon walls with deuterium fuel since it typically begins after about t = 30 s into the discharge, which is approximately the wall saturation time of deuterium in carbon [83]. The increased density and resistivity also rapidly consume the available inductive flux, which ultimately limits the pulse length.

With the recent change to a tungsten divertor, additional challenges need to be overcome to achieve ELM suppression and to extend high performance operation to long pulses in KSTAR. Excessive tungsten accumulation in the plasma core can quickly radiate away the plasma stored energy requiring real-time control of the tungsten source and impurity transport. RMP ELM suppression has proven difficult to achieve with a tungsten divertor.

Tungsten radiation can be mitigated by operating at higher density, but that regime is then incompatible with the low density RMP ELM suppression access as discussed in section 5. Nonetheless, new results with suppression of Type I ELMs, while not complete ELM suppression, has been obtained. Figure 16 shows a 32-second discharge (shot 36602) operated at $q_{95} \sim 6$ with $\beta_N \sim 2$ with a tungsten divertor, demonstrating complete suppression of all type-I ELMs using RMP. Despite successful type-I ELM suppression, small grassy ELMs persisted throughout the H-mode in all attempted control methods. The RMP spectrum was optimized with an edge-localized scheme, and RT-RMP control was not employed, since complete ELM suppression was not achieved. This ELM-mitigated regime with RMP was highly robust across multiple experimental days under various plasma conditions (different NBI configurations, plasma shapes, etc.). The primary physical constraints preventing longer pulse durations were flux consumption and nonlinear effects due to impurity radiation and transport. The use of long divertor gas puffs led to a gradual increase in density and a decrease in β_N.

High plasma performance long pulse operation with the tungsten divertor is difficult to maintain due to non-stationary radiated power fraction and plasma fueling control. Wall conditioning is essential to control the tungsten source. An impurity powder dropper (IPD) on KSTAR allows real-time control of low Z impurities dropped into the plasma to better control the tungsten source and the divertor radiation [84]. More robust control of impurities through IPD seems a promising route to extend the duration of ELM-controlled operations in the KSTAR tungsten environment. Such real-time wall conditioning and fueling control is expected to be important to improve stable long pulse operation in KSTAR as well as other tungsten PFC fusion devices such as ITER [85]. EAST has also struggled with density control, plasma current, and plasma equilibrium control and managed to overcome these issues for their record long pulse H-mode experiments, including enhanced magnetic diagnostic measurements [86] and the use of real-time lithium powder injection [87, 88].

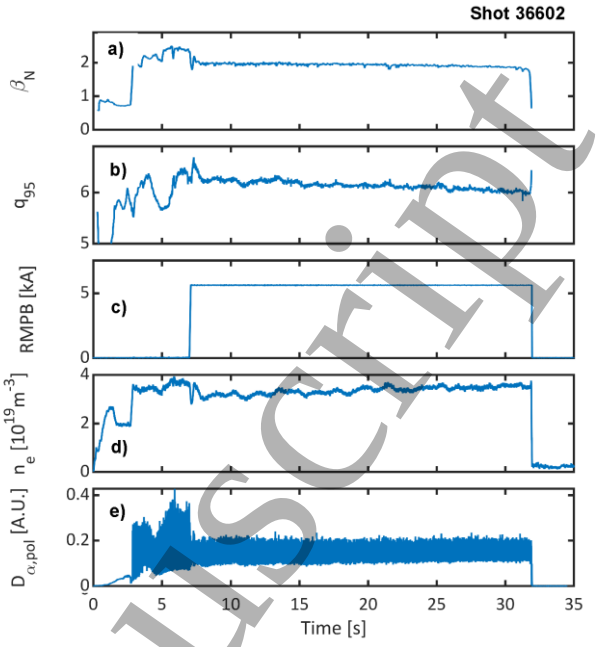

Figure 16. Time traces of KSTAR discharge #36602 showing a) β_N, b) q_{95}, c) bottom RMP coil current, d) line averaged electron density and e) D_α emission with Type I ELMs suppressed and remaining grassy ELMs mitigated during RMP.

8. Summary and future work

Substantial progress has been made developing sophisticated plasma control schemes with adaptive model-based control of the amplitude and phase of the three rows of RMP coils on KSTAR to tailor core and edge perturbed fields to simultaneously optimize ELM suppression, thermal and fast ion confinement, while avoiding core locked modes that could lead to disruptions. Ideal and kinetic models [49] are able to predict the optimum RMP coil current and phasing for a range of operational scenarios, which have been implemented into a

machine-learning based algorithm for real-time adaptive control that allows for long pulse high performance plasma operation with RMP ELM suppression. This physics-based model can also be applied to future burning plasma devices such as ITER and future fusion pilot plants.

The divertor heat flux striations due to RMP fields have also been successfully modeled taking into account the plasma response to RMP fields. Changes due to RMP fields to the erosion and redeposition of carbon of the previous carbon divertor in KSTAR have also been successfully modeled.

Through a database analysis from multiple tokamaks with RMP ELM control, the threshold metrics have been compared across devices for RMP ELM suppression. The operational space for RMP ELM suppression has also been mapped across multiple devices as well as the range of plasma performance that has been achieved.

Sophisticated modeling of the observed density pumpout with increasing RMP fields has successfully modeled even some nonlinear effects. The increased particle transport due to magnetic islands formed at the top of the edge pedestal have been modeled in reasonable agreement with experiment.

The integration of successful modeling of the RMP fields and the plasma response into sophisticated plasma control schemes has permitted the development of long pulse high plasma performance scenarios on KSTAR.

While substantial progress has been made developing high performance long pulse scenarios with ELM mitigation and suppression including control of the heat flux to PFCs and core radiation, the integration of these control schemes with divertor detachment control will be essential for high performance long pulse operation in a full tungsten environment. Such integrated control will be important for KSTAR, but also for future high performance tokamaks such as ITER and future Fusion Pilot Plants.

Acknowledgements

This work was supported by the U.S. Department of Energy under contract number DE-AC02-09CH11466 and DE-SC0021968. The United States Government retains a non-exclusive, paid-up, irrevocable, worldwide license to publish or reproduce the published form of this manuscript, or allow others to do so, for United States Government purposes. This research was also supported by R&D Program of "High Performance Tokamak Plasma Research & Development (EN2501-16)" through the Korea Institute of Fusion Energy (KFE) funded by the Government funds, Republic of Korea.

References

[1] J. D. Lawson, *Proc. Phys. Soc. B* **70**, 6 (1957).
[2] John Wesson, Tokamaks, Oxford University Press, Fourth Edition (2011).
[3] F. Wagner *et al* 1982 *Phys. Rev. Lett.* **49** 1408.
[4] C. Gormezano, *Plasma Phys. Control. Fusion* **41** (1999) B367–B380.
[5] R. J. Groebner, *et al, Nucl. Fusion* **41** (2001) 1789.
[6] F. Wagner, *Plasma Phys. Control. Fusion* **49** (2007) B1–B33.
[7] S. W. Yoon, *et al, Nucl. Fusion* **51** (2011) 113009.
[8] H. Zohm, *Plasma Phys. Control. Fusion* **38** (1996) 105–128.
[9] A. Loarte, *et al, Plasma Phys. Control. Fusion* **67** (2025) 065023.
[10] A. W. Leonard, *Phys. Plasmas* **21** (2014) 090501.
[11] Christopher Ham, Andrew Kirk, Stanislas Pamela, and Howard Wilson, *Nature Reviews Physics* **2** (2020) 159.
[12] K. H. Burrell, *et al, Plasma Phys. Control. Fusion* **44** (2002) A253–A263.
[13] T. E. Evans, *et al, Phys. Rev. Lett.* **92** (2004) 235003.
[14] M. Becoulet, *et al, Journal of Nuclear Materials* **337–339** (2005) 677–683.
[15] N. Oyama, *et al, Nucl. Fusion* **51** (2011) 033009.
[16] W. Suttrop, *et al, Phys. Rev. Lett.* **106** (2011) 225004.
[17] L. R. Baylor, *et al, Phys. Rev. Lett.* **110** (2013) 245001.
[18] I. T. Chapman, *et al, Plasma Phys. Control. Fusion* **58** (2016) 014017.
[19] J. K. Park, *et al, Nat. Phys.* **14** (2018) 1223-1228.
[20] S. M. Yang, *et al, Nucl. Fusion* **60** (2020) 096023.
[21] S. M. Yang, *et al, Nucl. Fusion* **63** (2023) 126046.
[22] S. M. Yang, *et al, Nature Comm.* **15** (2024) 1275.
[23] Yueqiang Liu, *et al, Nucl. Fusion* **64** (2024) 056005.

[24] Jong-Kyu Park, *Reviews of Modern Plasma Physics* **8** (2024) 1.
[25] S. M. Yang, *et al, Nucl. Fusion* **65** (2025) 096008.
[26] Minwoo Kim, *et al, Nucl. Fusion* **63** (2023) 086032.
[27] S. K. Kim, *et al, Nature Comm.* **15** (2025) 3990.
[28] R. Shousha, *et al, Nucl. Fusion* **65** (2025) 086021.
[29] H. Frerichs, *et al, Nuclear Materials and Energy* **34** (2023) 101380.
[30] Marcos Navarro, *et al, Phys. Plasmas* **31** (2024) 082508.
[31] N. C. Logan, *et al, Nucl. Fusion* **65** (2025) 076029.
[32] C. Paz-Soldan, *et al, Nucl. Fusion* **64** (2024) 096004.
[33] S. K. Kim, *et al, Nucl. Fus.* **63** (2023) 106013.
[34] Q. M. Hu, *et al, Nucl. Fusion* **63** (2023) 096002.
[35] Y. Liu, C. Paz-Soldan, L. I. Li, and Y. Sun, *Nucl. Fusion* **60** (2020) 036018.
[36] Xishuo Wei, *et al, Nucl. Fusion* **65** (2025) 026026.
[37] J. K. Park, et al, Proc. 29th IAEA Fusion Energy Conf., London (2023).
[38] H. K. Kim, *et al, Fusion Eng. Des.* **86** (2011) 1975.
[39] J. K. Park, A. H Boozer, and A. H. Glasser, *Phys. Plasmas* **14** (2007) 052110.
[40] T. Rhee, *et al, Phys. Plasmas* **26** (2019) 112504.
[41] Y. M. Jeon, *et al, Phys. Rev. Lett* **109** (2012) 035004.
[42] Y. In, *et al, Nucl. Fusion* **57** (2017) 116054.
[43] Y. Q. Liu, A. Bondeson, C. M. Fransson, B. Lennartson, and C. Breitholtz, *Phys. Plasmas* **7** (2000) 3681.
[44] Y. Q. Liu, M. S. Chu, I. T. Chapman, and T. C. Hender, *Phys. Plasmas* **15** (2008) 112503.
[45] M. J. Choi, *et al, Rev. Sci. Instrum.* **87** (2016) 013506
[46] Y. Q. Liu, P. B. Parks, C. Paz-Soldan, C. Kim, L. L. Lao, *Nucl. Fusion* **59** (2019) 126021.
[47] X. R. Li and V. Jilkov, *IEEE Trans. Aerosp. Electron. Syst.* **41** (2005) 1255.
[48] R. Shousha, 2018 Implementation of an imm kalman filter-based real-time event detector on the TCV tokamak *PhD Thesis* Eindhoven University of Technology (available at: https://research.tue.nl/en/studentTheses/implementationof-a-imm-kalman-filter-based-real-time-event-detec)
[49] G. Shin, J. W. Juhn, G. I. Kwon and S. H. Hahn, *Fusion Eng. Des.* **157** (2020) 11634.
[50] A. Loarte, *et al, Nucl. Fusion* **54** (2014) 033007.
[51] J. K. Park, *et al, Phys. Rev. Lett.* **126** (2021) 125001.
[52] P. N. Yushmanov, e*t al, Nucl. Fus.* **30** (1990) 1999.
[53] T. C. Luce, *et al, Nucl. Fusion* **43** (2003) 321.
[54] A. Kirk, *et al, Phys. Rev. Lett.* **108** (2012) 255003.
[55] T. E. Evans, *et al, J. Phys. Conf. Ser.* **7** (2005) 174.
[56] O. Schmitz, *et al, Plasma Phys. Control. Fusion* **50** (2008) 124029.
[57] M. W. Jakubowski, *et al, Nucl. Fusion* **49** (2009) 095013.
[58] J.-W. Ahn, *et al, Nucl. Fusion* **50** (2010) 045010.
[59] Y. Feng, F. Sardei, J. Kisslinger, *J. Nucl. Mater.* **266-269** (1999) 812.
[60] Y. Feng, *et al, Contrib. Plasma Phys.* **54 (4-6)** (2014) 426.
[61] H. Frerichs, *et al, Phys. Plasmas* **28** (2021) 102503.
[62] H. Frerichs, *Nucl. Fusion* **64** (2024) 106034.
[63] J. Romazanov, *et al, Nucl. Fusion* **62** (2022) 036011.
[64] J.-K. Park, *et al, Nucl. Fusion* **51** (2011) 023003.
[65] M. J. Schaffer, *et al, Nucl. Fusion* **48** (2008) 024004.
[66] G. Matsunaga, *et al, Fusion Eng. Des.* **98-99** (2015) 1113.
[67] E. J. Doyle, *et al, Nucl. Fusion* **47** (2007) S18.
[68] Y. Liu, *et al, Nucl. Fusion* **51** (2011) 083002.
[69] V. Rozhansky, *et al, Nucl. Fusion* **51** (2011) 083009.
[70] C. Paz-Soldan, *et al, Phys. Rev. Lett.* **114** (2015) 105001.
[71] C. Sung, *et al, Phys. Plasmas* **24** (2017) 112305.
[72] Robert Hager, C.S. Chang, N.M. Ferraro and R. Nazikian, *et al, Nucl. Fusion* **59** (2019) 126009.
[73] Q. Hu, *et al, Phys. Plasmas* **26** (2019) 120702.
[74] Q. Hu, *et al, Nucl. Fusion* **60** (2020) 076001.
[75] Z. Lin, T.S. Hahm, W.W. Lee, W.M. Tang and R.B. White *Science* **281** (1998) 1835–7.
[76] S. M. Yang, et al, *Phys. Rev. Lett*. **123** (2019) 095001.
[77] S. M. Yang, et al, *Nucl. Fusion* **61** (2021) 086009.
[78] Y.Q. Liu, A. Kirk, and Y. Sun, *Phys. Plasmas* **20** (2013) 042503.
[79] G. T. A. Huysmans, S. Pamela, E. van der Plas, and P. Ramet, *Plasma Phys. Control. Fusion* **51** (2009) 124012.
[80] M. Hoelzl, *et al, Nucl. Fusion* **61** (2021) 065001.
[81] G. McKee, *et al, Nucl. Fusion* **53** (2013) 113011.
[82] R. Fitzpatrick, *Phys. Plasmas* **5** (1998) 3325.
[83] Y. In, *et al, Nucl. Fusion* **59** (2019) 056009.
[84] Hanna Schamis, *et al, Nucl. Fusion* **65** (2025) 086037.
[85] J. A. Snipes, *et al, Nuclear Materials and Energy* **41** (2024) 101809.
[86] J. Huang, *et al, Phys. Plasmas* **30** (2023) 062504.
[87] W. Xu, *et al*, *Phys. Scr.* **96** (2021) 124034.
[88] Z. Wang, *et al, Nucl. Fusion* **65** (2025) 104001.